Multiphysics Simulation of In-Service Welding and Induction Preheating: Part 2

Part 2 complements the FEM developed in Part 1 by comparing simulated welding results with experiments to validate the model

BY K. C. RIFFEL, R. H. G. SILVA, A. J. RAMIREZ, A. F. F. ACUNA, G. DALPIAZ, AND M. T. P. PAES

Abstract

In-service welding simulations were carried out using a multiphysics finite element analysis (FEA). Calculated data as temperature and thermal cycles were validated by comparing them with experimental welding results carried out in a carbon steel pipe attached to a water loop. Two in-service welding cases were tested using the GMAW-P process with and without the assistance of induction preheating. The molten zone of weld macrographs and the simulated models were matched with excellent accuracy. The great agreement between the simulation and experimental molten zone generated a maximum error in the peak temperature of 1%, while in the cooling curve, the error was about 10% at lower temperatures. A higher hardness zone appeared in the weld's toe within the CGHAZ, where the maximum induction preheating temperature achieved was 90°C with a power of 35 kW. Induction preheating reduced the maximum hardness from 390 HV to 339 HV.

Keywords

- Type-B Sleeve Repair
- Welding Modeling
- Finite Element Analysis
- GMAW-P for In-Service Welding

Introduction

In-service welding is a very important demand in the oil and gas industry (Refs. 1–3). This welding technique aims to facilitate repairs and connection installations (hot tapping technique), besides mitigating pipeline downtime and keeping the system's operational capacity (Refs. 4–7). In-service welding is susceptible to a fast cooling rate due to the heat removal provided by the fluid flow inside the pipeline, making the weld metal and the heat-affected zone (HAZ) prone to the formation of brittle microstructures and defects like lack of fusion (Ref. 8). High-hardness microstructures like martensite in combination with a considerable amount of diffusible hydrogen make the joint susceptible to hydrogen-induced cracking (HIC). Boring and Bruce (Ref. 9), and Sabapathy et al (Ref. 10) address another concern regarding the in-service welding and the presence of high-pressure flow which can lead to burnthrough/blowout if the heat input is not controlled.

The procedure qualification for in-service welding involves the mounting of complex fluid circulation systems (loop) to emulate a severe heat transfer condition as specified in the API 1104 Appendix B (Ref. 6). Chaowen and Yong (Ref. 11) and Wang et al. (Ref. 12) present three different water loop systems manufactured to induce forced convection in the part wall and create a high heat flux condition. The qualification relies on the HAZ and mechanical properties of the welding, which are dependent on the thermal cycle and cooling rate of the microstructure. For carbon steels, the cooling time is typically evaluated at the range between 800°C and 500°C, and this time is also known as $\Delta t_{8\text{-}5}$. Above this range is where austenite is transformed into stable phases at lower temperatures, such as martensite, bainite, and ferrite (Refs. 13, 14).

In this context, the welding parameters, material composition, preheating techniques, and fluid flow conditions are the factors that control the thermal dynamics of the procedure resulting in a determined final microstructure and welding bead. From the process point of view, the parameters such as welding current, voltage, welding speed, and heat input determine the temperature distribution and thermal cycle put in the part. Due to the several factors, parameters, and variables present in in-service welding, it is important to employ methods for the predictability of results as a function of certain input parameters. This approach enables an understanding of physical phenomena that are difficult to measure or test, as well as providing potentially more dynamic testing procedures, reducing time and raw material costs.

https://doi.org/10.29391/2024.103.008

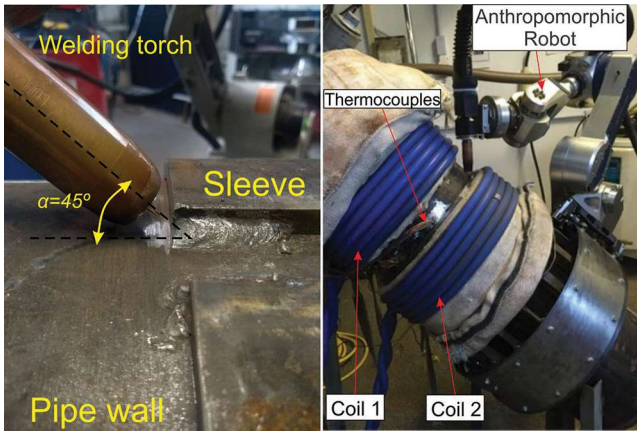

Fig. 1 — Experimental setup for automated in-service welding of Type-B sleeve.

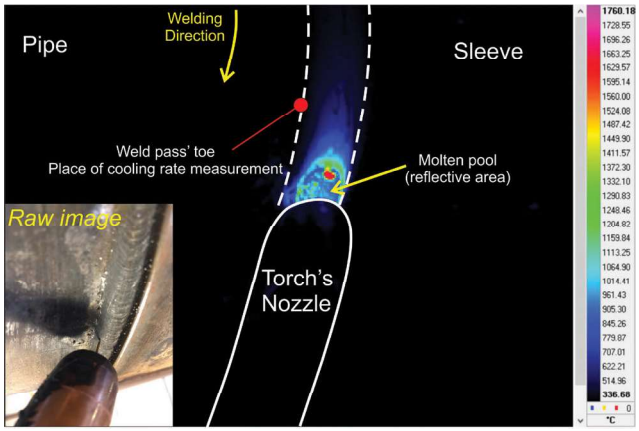

Fig. 2 — Example of thermography image applied to evaluate temperature and Δt_{8-5} during the tests.

Therefore, part 1 of this paper presented the implementation of a multiphysics model using the finite element method (FEM) for in-service welding, besides providing the mathematical equations and a discussion on the simulation post-processing results. Guest et al. [Ref. 15] applied the FEM to simulate the in-service welding and calculate the thermal history on a specific point of the microstructure, as well as the Δt_{8-5}. Huang et al. (Ref. 16) applied the FEM to simulate a very simplified bead-on-pipe condition in which the temperature distribution was estimated based on the welding heat input. Alian et al. (Ref. 17) developed a thermo-mechanical finite element analysis (FEA) for in-service welding aiming to verify the influence of the welding sequence over the circumferential distortion and residual stress in the pipe. Wang et al. (Ref. 12) created a model to analyze temperature distribution and thermal cycles for in-service fillet welding of type-B sleeves. The authors proposed a comparison of the cooling rate of the welding depending on the convective flux of different fluids. Most of the papers in the literature created thermal models to analyze the temperature distribution, but in all cases, very important variables were simplified. For instance, the preheating temperature, welding joint geometry, fluid flow, and the internal heat transfer coefficient (*h*). Nevertheless, this last one is presented as a constant value and based on a fully developed flow (completely different behavior compared to a reduced pipe length considered in welding qualifications). Moreover, a weak correlation between the simulated welding thermal cycles and welding molten zone with experiments was shown by the authors.

Thus, this paper presents simulation results and validation of the multiphysics in-service welding model from part 1, comparing post-processing results with experimental data (Ref. 18). The innovative use of the GMAW process with pulsed current (GMAW-P) as an alternative for circumferential in-service welding of type-B sleeves is also discussed. According to Dutra et al. (Ref. 19) and Palani and Murugan (Ref. 20) the GMAW-P can allow more flexibility in terms of heat input to the part, giving a greater parameterization range, control alternatives, and higher productivity since most of the in-service welding is carried out using the Shielded Metal Arc Welding (SMAW).

Experimental Procedure

Materials and Equipment

A detailed schematic of the experimental setup was explained in part 1 of this research, in which a water loop was mounted to emulate the greater heat flux faced in pipelines under operation (Ref. 18). The mock-up was a carbon steel pipe API 5L grade B with 2 m in length, 324 mm in diameter, and 9.5 mm thick. Its basic microstructure was composed of ferrite and perlite and the chemical composition is presented in Table 1. The type-B sleeve was manufactured using the same material as the pipe and then fitted around its circumference. Figure 1 shows the experimental setup detailed in the schematic of part 1, the image also details the torch's positioning and the thermocouples attachment for temperature monitoring. The filler metal was an AWS ER 70S-6 of 1.2 mm in diameter with its chemical composition also presented in Table 1.

The water flow was set to 380 l/min measured using a flowmeter. The water temperature was kept at 20°C. The induction preheating coils were set around the pipe and the sleeve. Three welding beads were deposited to complete the joint following the downhill direction. The welding started at 12 o'clock position up to 6 o'clock.

Two conditions were experimentally tested to compare and validate the simulation: 1. Circumferential welding without induction preheating (coils in mode off); and 2. Circumferential welding assisted by induction preheating (coils in mode on). As also stated in the model setting discussion of part 1, the maximum temperature was controlled at 400°C on the sleeve, and in the pipe, the temperature hit was 90°C. Due to convection heat transfer inside the pipe, the temperature on its surface was lower than in the sleeve. The sleeve can be considered partially insulated from the pipe due to an air gap between both parts making it easier to reach higher temperatures.

The induction power source was a Miller Pro Heat 35 kW with two flexible copper cables (coils) of 10 mm in diameter. The welding was carried out by an anthropomorphic robot,

Table 1 — The Chemical Compositions of the API 5L B Grade and AWS ER 70S-6 Measured Using Spectrometry

Material	C	Mn	Si	P	S	Cr	Ni	Fe	CE_{IIW}
API 5L B grade	0.23	0.92	0.05	0.02	0.01	0.02	0.01	Bal.	0.39
AWS ER 70S-6	0.09	1.14	0.64	0.01	0.01	0.02	0.06	Bal.	0.40

Table 2 — Parameters Applied to the Circumferential Weld

Parameters of GMAW-P	
Pulse current (*Ip*)	380 A
Pulse time (*tp*)	2.7 ms
Background current (*Ib*)	60 A
Background time (*tb*)	3.5 ms
Average current (*Im*)	200 A
Average voltage (*Um*)	26.0 V
Average power (*Pm*)	6060 W
Wire feed speed (WFS)	6 m/min
Contact tip to work distance (CTWD)	17 mm
Travel speed (Ts)	30 cm/min
Shielding gas	Ar + 8%CO_2

using the GMAW-P. The process was parametrized in preliminary tests and its parameters are presented in Table 2.

Temperature and thermal cycles were measured during the circumferential welding using type-K thermocouples attached as near as possible to the arc's path. Only the thermal cycle with the highest temperature in each one of the three welding beads was considered in the FEA comparison. Due to cooling characteristics that will be discussed in the results section, the Δt_{8-5} was measured in the weld pass' toe, as pointed out in Fig. 2. Thermography was applied according to Fig. 2, in which the image temperature was calibrated using the thermocouples attached to the part, once the emissivity was assumed constant at the value of 0,73, which represented more realistic the pipe's wall temperature although the molten pool's temperature is below the real value due to its reflectivity. The temperature range selected in the FLIR SC7200 heat camera was the option from 300°C up to 3000°C.

After finishing the welding, the joint was cut and prepared for micrographic analysis. The samples were etched using Nital 2% using the swabbing technique for 15 s. Each welding condition was compared to the simulations developed on COMSOL Multiphysics 6.1 by means of the molten zone area, the heat-affected zone (HAZ), and the thermal cycles. Microhardness indentations ($HV_{0,2}$) were carried out to evaluate the microstructure using a Leco LM 100AT with a load of 200 g and 150 µm of spacing between indentations. Microstructural analyses of experimental welds were also performed using a Leco Olympus GX50 optical microscope and a continuous cooling transformation (CCT) diagram was simulated for the API 5L B grade using the software JMatPro 12. The grain size of the base material was an input parameter to the CCT simulation, which was measured according to ASTM E112 (Ref. 21) with an average size of 21 µm.

Results and Discussion

Thermal FEA of the Model for In-Service Welding

Results and discussion are based on the reduced-scale model presented in part 1 of this paper (Ref. 18). Figure 3 shows the transient evolution of the temperature during the preheating up to the regime condition, in which the model greatly met the experimental temperature. The sleeve maximum temperature is at 400°C right beneath the center of the coil. On the pipe wall, the maximum temperature was 115°C beneath the coil and about 90°C in the joint location.

Figure 4 presents a transient evaluation of circumferential welding comparing preheated versus not preheated cases at the times of 10 s, 25 s, and 45 s. The condition with preheating exhibited a lower temperature gradient due to the higher initial condition. The induction heating was kept during the whole welding, while its temperature increase can provide higher hydrogen diffusion even at regions far from the weld. Literature shows that an increase in the part temperature can avoid cold cracking due to the mitigation of diffusible hydrogen within the welded joint (Refs. 22, 23). Coe (Ref. 24), for example, presents that by increasing the part temperature to 100°C, the hydrogen diffusivity coefficient increases by 1000 times compared to a room temperature of 20°C.

Figures 5 and 6 compare the weld macrograph versus the simulation (with and without induction heating). Black dashed lines in the macrograph represent the contour of the welding

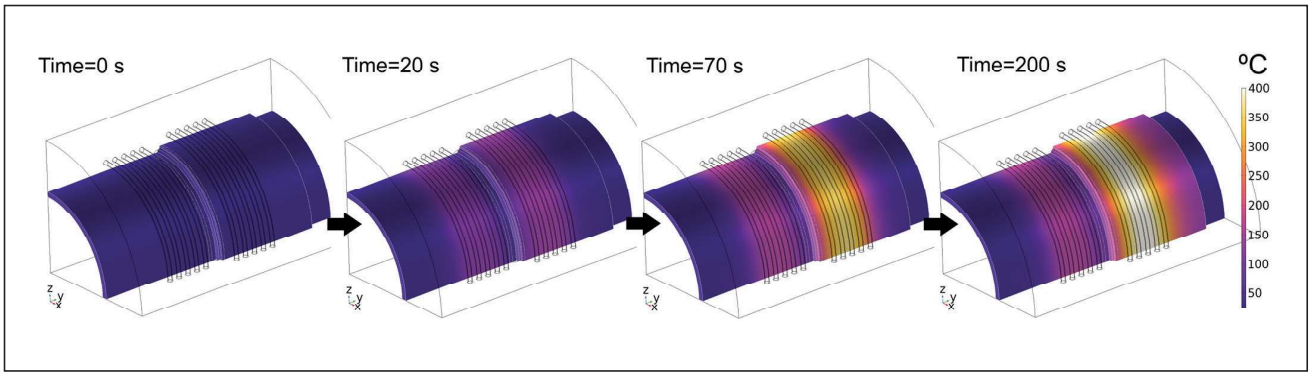

Fig. 3 — Transient analysis of induction preheating up to the temperature regime and the time of 200 s.

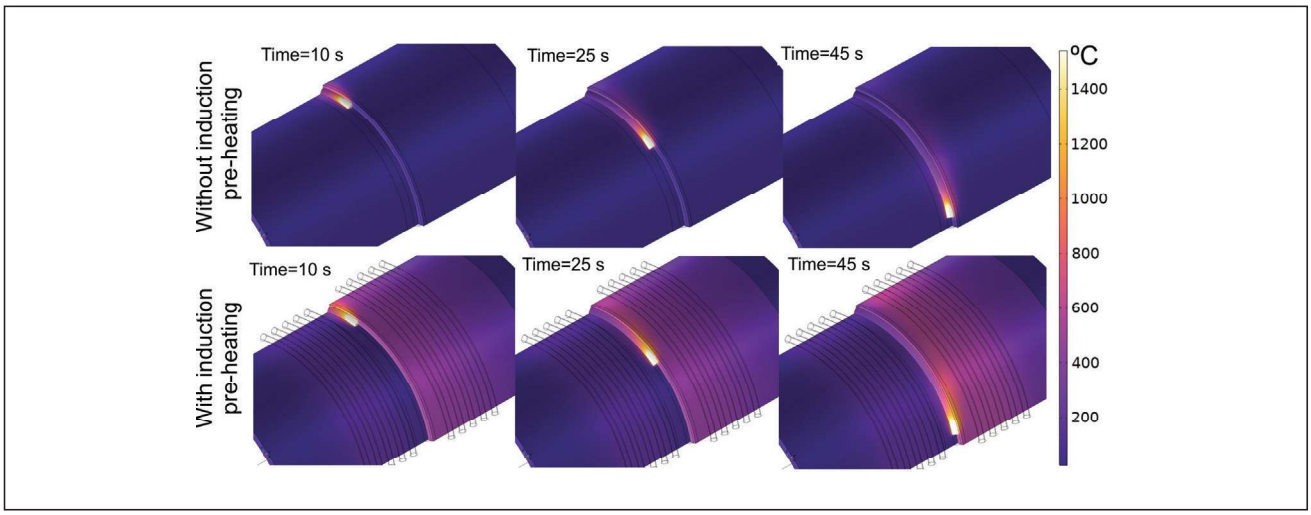

Fig. 4 — Transient temperature analysis of the circumferential welding simulation comparing conditions with and without induction preheating.

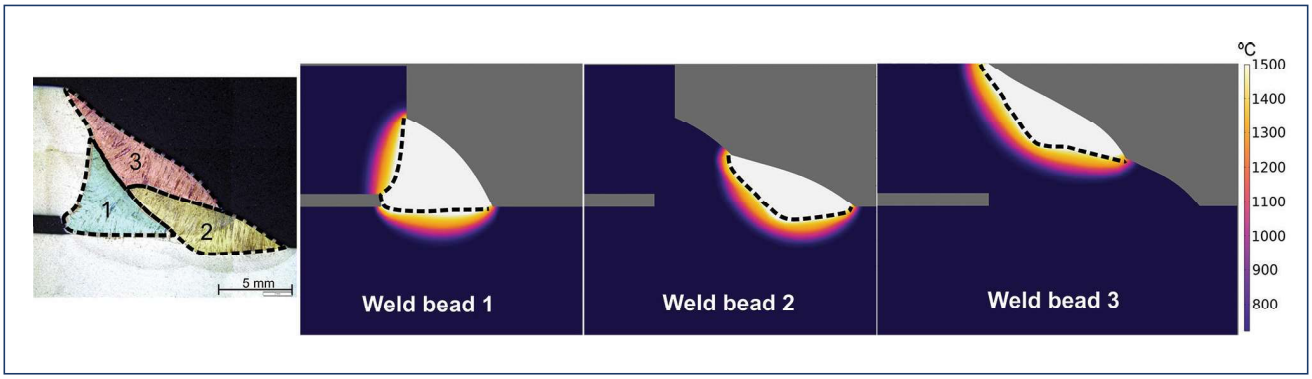

Fig. 5 — Welding macrograph of GMAW-P without induction preheating and comparison of the molten zone and heat-affected zone of experimental results versus simulated welding bead.

metal (molten zone) for each weld bead. The maximum error in the molten area was 8.1% (without pre-heating), while for the pre-heated condition, the error was 13.2%. Considering all three passes, the error in the molten zone was at the average of 6.2% (without pre-heating) and 10.6% (pre-heated). From the double ellipsoid volumetric distribution, shown in part 1 of this work, the error reduction can be obtained by a combination of more than one heat source followed by the adjustment of its dimensions in comparison with the experimental molten zone, as a form of calibration. This method of calibration comparing the experimental molten zone with the simulated one was also applied by Kik (Ref. 25) and Farias et al. (Ref. 26), which addresses the generic simulation of the welding process. However, specifically within the simulation

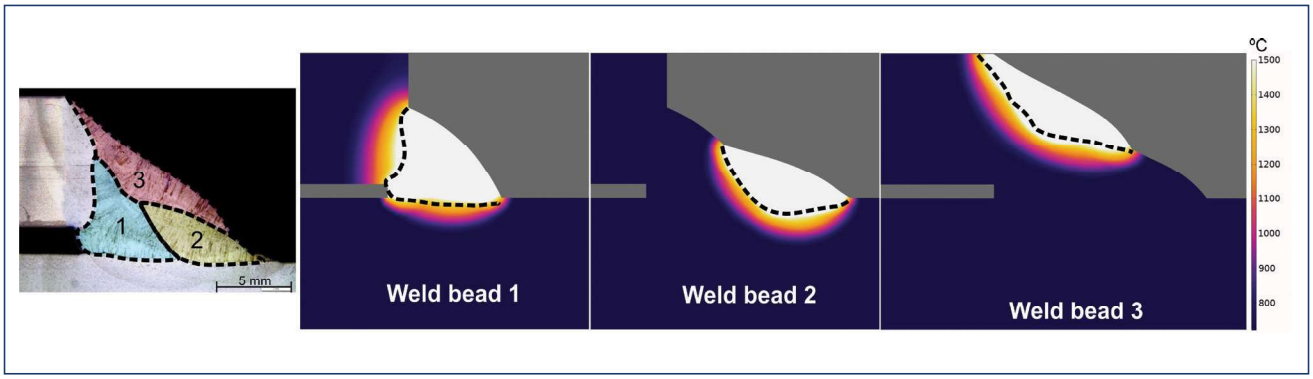

Fig. 6 — Welding macrograph of GMAW-P with induction pre-heating and comparison of the molten zone and heat-affected zone of experimental results versus simulated welding bead.

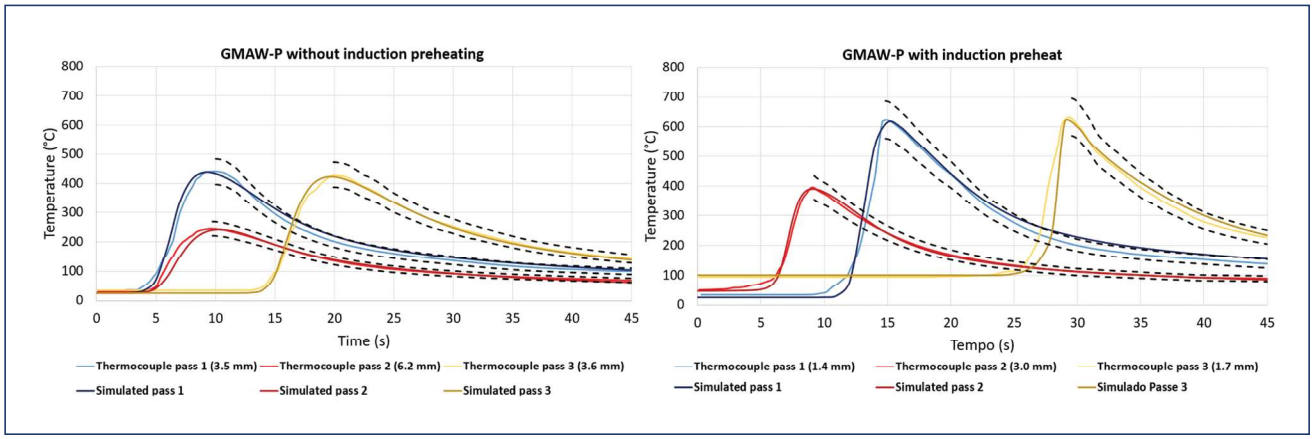

Fig. 7 — Comparison of experimentally acquired thermal cycles versus simulated probes at the same distance from the welding bead.

of in-service welding, few works present a comparison of the simulated molten zone with the experimental results (Refs. 15–17). In comparison with the work by Mondal et al. (Ref. 27), which developed a source profile calibration for welding simulation, the fit reached in this work showed an excellent representation of the experimental molten area with relatively low error.

The second comparison index between the model and experimental results was the measured thermal cycles. Excellent agreement was obtained between thermocouples and the virtual probes in the model. Figure 7 presents a comparison of the highest peak temperature measured experimentally with the simulations and the distance of the thermocouples to the weld bead's toe measured after its deposition (distance in the graph's captions). The dashed lines in Fig. 7 represent an error of ±10% around the tail out of the curve. The maximum error verified was about 10% in the first bead, but only in a temperature range near 300°C where the tail out of the simulated curve touches the dashed line. The error in the peak temperature was about 1%.

The temperature gradient (*dT/dx*) is very high in high-cooling circumstances (hundreds of °C per millimeter), making it very difficult to measure high-temperature values without burning the thermocouple with the arc during the welding (if the thermocouple is too near the weld bead's toe).

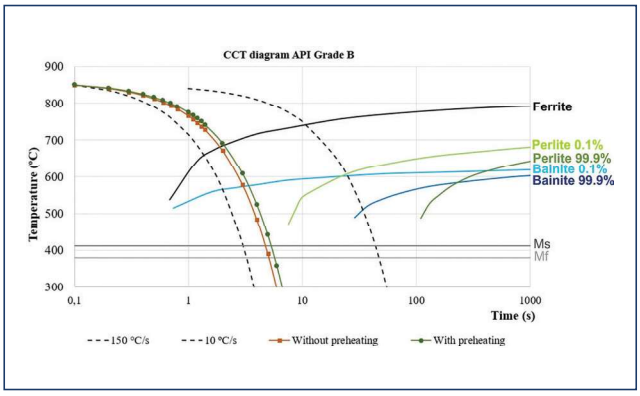

Fig. 8 — Simulated cooling curves based on the simulated Δt_{8-5} plotted over the CCT diagram of base material.

According to the acquired peak temperature, any remaining thermocouple measured a value over 800°C complicating the straight capture of the Δt_{8-5}. Thus, the simulation can be used to extrapolate the cooling curves to higher peak temperatures, once the model is calibrated with lower-tem-

Table 3 — Cooling Times Δt_{8-5} and Cooling Rate Comparing Conditions With and Without Induction Preheating

Δt_{8-5} (s)						
Without Preheating				With Induction Preheating		
Pass	Thermography	Simulation	Simulated Cooling Rate (°C/s)	Thermography	Simulation	Simulated Cooling Rate (°C/s)
1	3.8	3.6	83.3	4.1	4.0	75.0
2	3.2	3.2	93.7	5.1	3.6	83.3
3	4.7	4.1	73.1	7.6	6.6	45.5

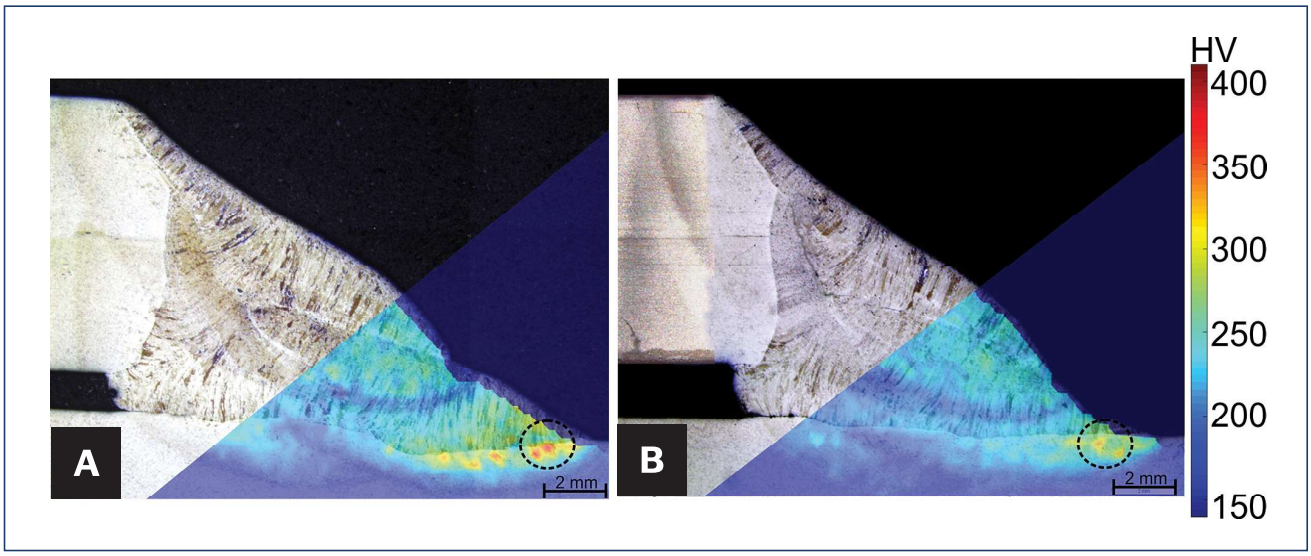

Fig. 9 — Microhardness maps plotted over macrographs in: A — Condition without induction preheating with a maximum hardness of 390 HV; B — condition with 90°C of induction preheating with a maximum hardness of 339 HV.

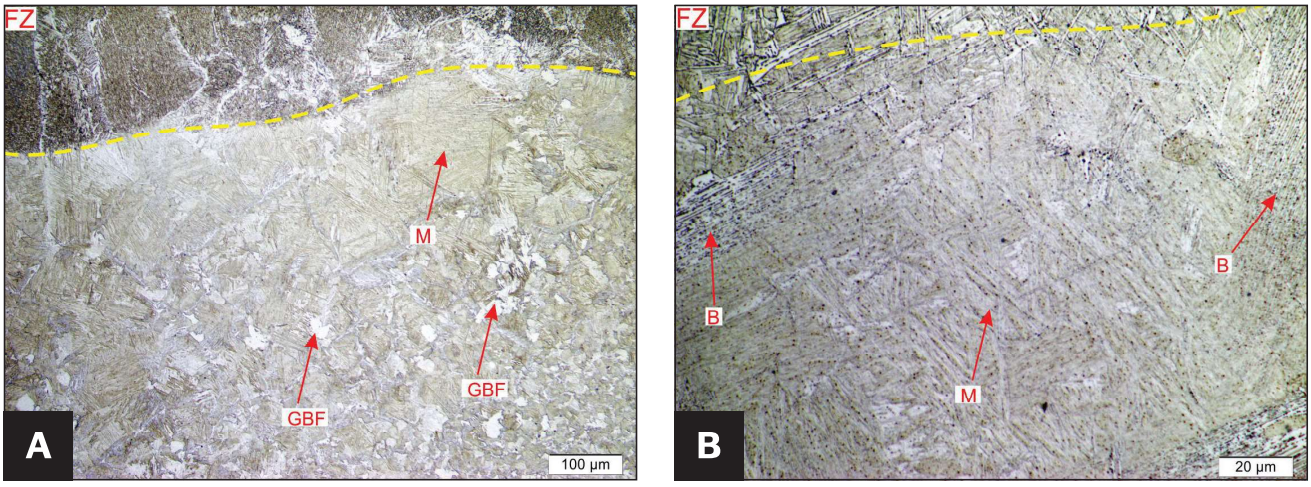

Fig. 10 — Microstructural analysis of the high-hardness zone for the condition without induction preheating in: A — 200× magnification; B — 1000× magnification.

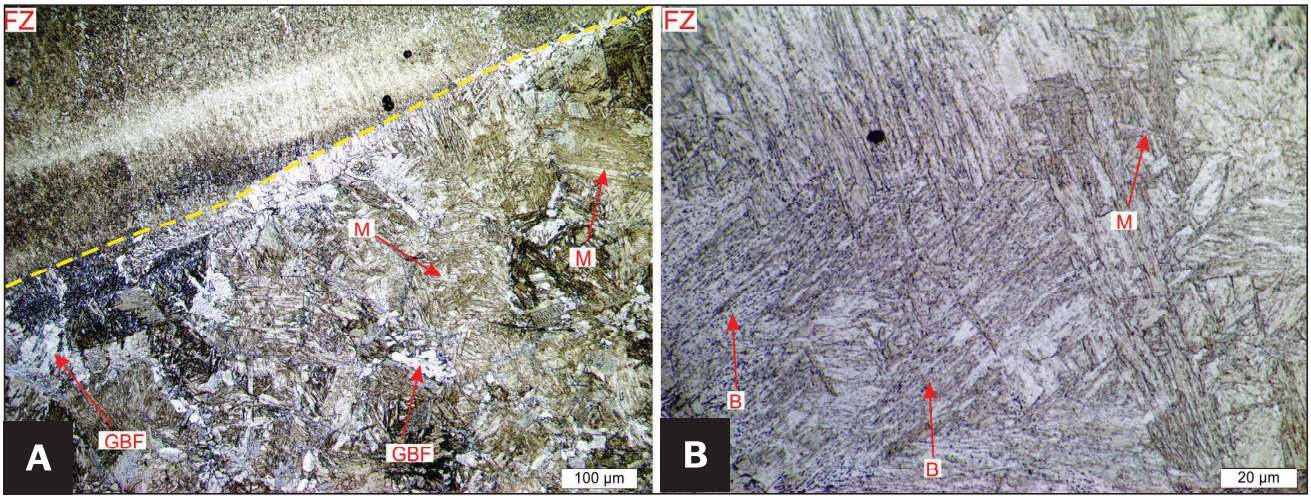

Fig. 11 — Microstructural analysis of the high-hardness zone for the condition with induction preheating in: A — 200× magnification; B — 1000× magnification.

perature thermal cycles, cross-section molten zone, and temperature distribution.

The greater error verified at lower temperatures in the tail-out of thermal cycles (Fig. 7) is related to the cooling rate difference between experiments and simulation. The cooling rate is a function of the convection heat transfer between the pipe wall and the fluid flow, as well as the conduction through the pipe and the sleeve. One source of error can arise from the physical properties of the materials considered in the simulation shown in Part 1 of this paper (Ref. 18). The values considered in the model represent the ones identified for generic carbon steels and a slight difference in thermal conductivity at a specific temperature range, for example, can affect the heat diffεεusion and consequently the cooling rate. The chemical composition directly affects physical properties. It is quite complex in a model to consider all the existing phenomena and variations faced in experimental conditions. Other factors that can contribute to the error in the cooling rate are effects related to changes in the fluid flow profile inside the pipe and changes in its properties as a function of the temperature, locally affecting the cooling rate.

To reduce this error in the cooling rate, one alternative would be to measure the physical properties of the material specifically for the chemical composition used in this work. Another approach could be the use of a feedback simulation (closed loop) that compares the experimental versus simulated cooling rates and adjusts the material properties until the thermal cycles match (a form of calibration). Thus, the model's error could be reduced. Similarly, a different flow model than the k-ε could be tested to capture the fluid flow movement and the variation of the heat transfer coefficient more accurately with temperature, as shown in Part 1 (Ref. 18).

Microstructural Evaluation and Microhardness Maps of the In-Service Welding

Using thermography, it was possible to measure temperatures higher than the ones measured by thermocouples, right on the weld's toe, enabling the direct measurement of the $\Delta t_{8\text{-}5}$. Table 3 compares the $\Delta t_{8\text{-}5}$ from thermography with thermal cycles extrapolated from simulation. The values are very close for both cases considering that the thermography has a constant emissivity which can induce an error in the temperature. The maximum error for all weld beads was 1 s in the third pass of preheated case. Corroboration with empirical results indicates reliability in the methodology and in the model to predict cooling times and temperature distribution for in-service welding qualification.

Table 3 shows that the faster cooling rate was measured on the second pass' toe for both conditions. According to the welding sequence presented in part 1 of this paper, the second pass is deposited right over the pipe wall, getting more effect of the forced convection heat flux, and resulting in a faster cooling rate. Plotting the shorter simulated $\Delta t_{8\text{-}5}$ (in the second pass of Table 3) over the simulated CCT diagram of the base material, its microstructure was estimated in Fig. 8. The major area of interest was the coarse grain HAZ (CGHAZ) where the heating above the austenitization can transform the austenite into martensite upon cooling, according to the literature (Ref. 8). The greater the % C available on the base metal, the harder the microstructure is due to the higher amount of carbon available for martensite formation within the grains in the heat-affected zone (Ref. 28). High hardness zones can indicate a very brittle microstructure and higher susceptibility to HIC. Analyzing the diagram in Fig. 8, a mix of ferrite, bainite, and martensite was predicted for both conditions (with and without preheating). The preheating at 90°C reached using 35 kW in the second pass's toe barely changed the cooling rate at high temperatures and the microstructure was slightly affected due to the small shift in the cooling curve of Fig. 8.

Microhardness maps merged with the welding macrographs indicated high hardness microstructure located in the CGHAZ, according to the dashed area in Fig. 9. Even though the microstructure of the induction preheated condition was like the condition without induction, as pointed out in the CCT diagram of Fig. 8, the maximum hardness was lower. The hardness peak was reduced from 390 HV to 339 HV using the

induction preheating at 90°C. Such a change in the hardness value makes the condition with induction heating acceptable in standard requirements, according to API 1104 (Ref. 6), which stipulates a maximum of 350 HV for such carbon steel pipes. The hardness reduction suggests that even a small increase in the Δt_{8-5} can enable more time for ferrite growth, and consequently a more ductile microstructure.

An analysis of the high hardness area confirmed the presence of the three main microstructures predicted in the CCT diagram, as shown in the optical microscopy images in Figs. 10 and 11. Figs. 10A and 11A show the interface between the fusion zone and the CGHAZ, in which is possible to verify a structure composed of grain boundary ferrite (GBF) and martensitic grains. The microstructure is mainly martensitic in the middle of the coarser grains (needles-like morphology). With the higher magnification in Figs. 10B and 11B, it is also verified some fine bainitic structure, which is expected for the composition of the base material.

It can also be stated that with different welding parameters than those presented in Table 2 (for example, different average current, wire speed, and welding speed), the heat input to the pipe would change. For in-service welding, a lower heat input would result in faster cooling of the microstructure for the same fluid flow, affecting the Δt_{8-5} and consequently increasing the microstructure's hardness. Lower welding energies would also impact the process quality, increasing susceptibility to defects such as lack of fusion. On the other hand, using a higher heat input would have the opposite effect making it easier to obtain a more ductile microstructure. However, in practical terms, it would complicate the control of the molten pool in critical welding positions such as vertical and overhead.

Conclusions

This paper was the second and final part of a work developed to study a model for in-service welding using a multiphysics proposition. Part 2 focused on the temperature distribution results of the post-processing and the comparison between experimental results with simulated ones. From this paper, the following conclusions can be stated:

- Calibrating the simulated molten zone based on welding macrographs guaranteed excellent agreement between simulated thermal cycles, and peak temperature measurements with thermocouples. The maximum error in the tail out of the thermal cycles was about 10% at lower temperatures, while in the peak temperature, the error was about 1%.
- For the in-service welding of type-B sleeves following the sequence proposed in this work, the last pass deposited over the pipe is the one that faces the faster cooling rate because of the forced convection.
- The Δt_{8-5} was 3.2 s without induction and 3.6 s with induction preheating of 90°C, for both cases, the microstructure was a mix of ferrite, martensite, and bainite. Thus, this level of preheating barely changed the microstructure, even though the maximum hardness was reduced from 390 HV to 339 HV (meeting standard requirements).
- From a practical standpoint, the use of induction heating coupled with the proposed multiphysics simulation has the potential to achieve a better approximation between the qualification proposed in standards and real repair welds by considering the preheating thermal source. On the other hand, preheat temperatures higher than 90°C may be necessary to adequately control the cooling rate, especially for pipes with higher %C, albeit avoiding the risk of pipeline burn through/blowout.
- Future publications will explore the mechanical behavior of the welded joint, considering the residual stress and deformation.

References

1. Bruce, W. A. 2002. Qualification of procedures for welding onto in-service pipelines. *Proceedings of the 4th International Pipeline Conference.* Calgary, Alberta, Canada. September 29 – October 3: 39–53. ASME. DOI: 10.1115/IPC2002-27131

2. Bruce, W. A., Holdren, R. L., Mohr, W. C., and Kiefner, J. F. 1996. Repair of pipelines by direct deposition of weld metal further studies. *Final Report.* https://www.osti.gov/biblio/576170.

3. Tronskar, J. P., Tornqvist, R., Guan, O. H., and Bruce, W. A. 2015. "Live" repair of gas pipeline with deep girth weld crack. *Proceedings of the ASME 2015 Pressure Vessel and Piping Conference*, July 19–13. Boston, Massachusetts, USA. DOI: 10.1115/PVP2015-46005

4. Batisse, R., and Hertz-Clemens, S. A. 2008. Review of various repair techniques for gas transmission pipelines: advantages, limitations, and developments. *GFD SUEZ FRANCE. International Gas Union Research Conference*, Paris. DOI: 10.1007/978-1-4020-6526-2_20

5. Farzadi. A. 2016. Gas pipeline failure caused by in-service welding. *Journal of Pressure Vessel Technology* February 138(1). DOI: 10.1115/1.4031443

6. API 1104. 2007. Standard for welding pipelines and related facilities. *American Petroleum Institute* 50.

7. Jaske, C. E., Hart, B. O., and Bruce, W. A. 2006. Pipeline repair manual – revision 6. *Pipeline Research Council International (PRCI)*. Arlington, Virginia.

8. Bruce, W. A., and Bradley, C. E. 2012. Further development of heat-affecter zone hardness limits for in-service welding. *Proceedings of the 2012 9th International Pipeline Conference*. September 24–28. Calgary, Alberta Canada. DOI: 10.1115/IPC2012-90095

9. Boring, M. A., and Bruce, W. A. 2008. The effect of hoop stress on the burnthrough susceptibility during in-service welding of thin-walled pipelines. *Proceedings of 7th International Pipeline Conference*. September 29–October. Calgary, Alberta, Canada. DOI: 10.1115/IPC2008-64354

10. Sabapathy, P. N., Wahab, M. A., and Painter. M. J. 2000. The prediction of burn-through during in-service welding of gas pipelines. *International Journal of Pressure Vessels and Piping* 77: 669–677. DOI: 10.1016/S0308-0161(00)00056-9

11. Chaowen, L., and Yong, W. 2013. Three-dimensional finite element analysis of temperature and stress distributions for in-service welding process. *Materials and Design* 52: 1052–1057. DOI: 10.1016/j.matdes.2013.06.042

12. Wang, Y., Wang, L., Di, X., Shi, Y., Bao, X., and Gao, X. 2013. Simulation and analysis of temperature field for in-service multi-pass welding of a sleeve fillet weld. *Computational Materials Science* 68: 198–205. DOI: 10.1016/j.commatsci.2012.10.025

13. Meszaros, K., Vrolyk. C., Pepin, J., Yamuch. M., and Mah-Paulson, T. 2012. The effects of temper bead welding technique on weld integrity for in-service welding of carbon steels. *Proceedings of the 2012 9th International Pipeline Conference*. Calgary, Alberta, Canada. DOI: 10.1115/IPC2012-90242

14. Turichin, G., Kuznetsova, M., Pozdnyakova, A., Gookc, S., Gumenyukd, A., and Rethmeierd, M. 2018. Influence of heat input and preheating on the cooling rate, microstructure and mechan-

ical properties at the hybrid laser-arc welding of api 5l x80 steel. *Proceedings of the 10th CIRP Conference on Photonic Technologies* 748: 751. DOI: 10.1016/j.procir.2018.08.018

15. Guest, S., Dyck, J., Egbewande, A., Mackenzie, R., and Sadowski, M. 2016. Design of in-service repair welding procedures for operating pipelines: critical assessment of variables affecting restraint level and heat-affected zone microstructures of vintage pipelines. *Proceedings of the 2016 11th International Pipeline Conference.* September 26–30, Calgary, Alberta, Canada. DOI: 10.1115/IPC2016-64206

16. Huang, Z., Tanga, H., Dingb, Y., Weic, O., and Xiac, G. 2017. Numerical Simulations of temperature for the in-service welding of gas pipeline. *Journal of Materials Processing Technology* 248: 72–78. DOI: 10.1016/j.jmatprotec.2017.05.008

17. Alian, A. R., Shazly, M., and Megahed. M. M. 2016. 3D finite element modeling of in-service sleeve repair welding of gas pipelines. *International Journal of Pressure Vessels and Piping* 146: 216–229. DOI: 10.1016/j.ijpvp.2016.09.002

18. Riffel, K. C., Silva, R. H. G., Ramirez, A. J., Acuna, A. F. F., Dalpiaz, G., and Paes, M. T. P. 2023. Multiphysics simulation of in-service welding and induction preheating: Part 1. *Welding Journal*.

19. Dutra, J. C., Silva, R. H. G., Savi, B. M., Marques, C., and Alarcon, O. E. 2015. New methodology for ac-pulsed gmaw parameterization applied to aluminum shipbuilding. *Journal of the Brazilian Society of Mechanical Sciences and Engineering* 38: 99–107. https://link.springer.com/article/10.1007/s40430-015-0351-3

20. Palani, P. K., and Murugan, N. 2006. Selection of parameters of pulsed current gas metal arc welding. *Journal of Materials Processing Technology* 172 (1): 1–10. DOI: 10.1016/j.jmatprotec.2005.07.013

21. ASTM E112-13. Standard test methods for determining average grain size. Available on: https://www.astm.org/e0112-13r21.html.

22. Gaillard, R., Debiez, S., Hubert, M., and Defourny, J. 1988. Methods for optimizing the preheat temperature in welding. *Welding in the World* 26(9/10): 216–230.

23. Meszaros, K., Vrolyk. C., Pepin, J., Yamuch., M., and Mah-Paulson, T. 2012. The effects of temper bead welding technique on weld integrity for in-service welding of carbon steels. *Proceedings of the 2012 9th International Pipeline Conference*. Calgary, Alberta, Canada. DOI: 10.1115/IPC2012-90242

24. Coe, F. R. 1973. Welding steels without hydrogen cracking. *Welding Institute* 68 Cambridge, UK.

25. Kik, T. 2020. Heat source models in numerical simulations of laser welding. ***Materials*** 13(11): 2653. DOI: 10.3390/ma13112653

26. Farias, R. M., Teixeira, P. R. F., and Vilarinho, L. O. 2022. Variable profile heat source models for numerical simulations of arc welding processes. *International Journal of Thermal Sciences* 179: 107593. DOI: 10.1016/j.ijthermalsci.2022.107593

27. Mondal, A. K., Kumar, B., Bag, S., Nirsanametla, Y., and Biswas, P. 2021. Development of avocado shape heat source model for finite element based heat transfer analysis of high-velocity arc welding process. *International Journal of Thermal Sciences* 166: 1070005. DOI: 10.1016/j.ijthermalsci.2021.107005

28. Lippold, J. C. Chapter 5- hydrogen-induced cracking. *Welding Metallurgy and Weldability* 213–262. DOI: 10.1002/9781118960332.ch5

KAUE CORREA RIFFEL (*riffel.12@osu.edu*) and **REGIS HENRIQUE GONÇALVES E SILVA** are with the Federal University of Santa Catarina, Florianopolis, Santa Catarina, Brazil. **ANTONIO JOSE RAMIREZ** and **ANDRES FABRICIO FISCHDICK ACUNA** are with The Ohio State University, Columbus, Ohio. **GIOVANI DALPIAZ** and **MARCELO TORRES PIZA PAES** are with Petrobras/CENPES, Rio de Janeiro, Brazil.